Discrete dislocation analysis of size effects in thin films

Nicola, Lucia; Van der Giessen, Erik; Needleman, Alan

Link to publication in University of Groningen/UMCG research database

Discrete dislocation analysis of size effects in thin films

Lucia Nicola and Erik Van der Giessen[a]
The Netherlands Institute for Metals Research/ Department of Applied Physics, University of Groningen, Nyenborgh 4, 9747 AG Groningen, The Netherlands

Alan Needleman
Division of Engineering, Brown University, Providence, Rhode Island 02912

A discrete dislocation plasticity analysis of plastic deformation in metal thin films caused by thermal stress is carried out. The calculations use a two-dimensional plane-strain formulation with only edge dislocations. Single crystal films with a specified set of slip systems are considered. The film-substrate system is subjected to a prescribed temperature history and a boundary value problem is formulated and solved for the evolution of the stress field and for the evolution of the dislocations structure in the film. A hard boundary layer forms at the interface between the film and the substrate, which does not scale with the film thickness and thus gives rise to a size effect. It is found that a reduction in the rate of dislocation nucleation can occur abruptly, which gives rise to a two-stage hardening behavior. © *2003 American Institute of Physics.* [DOI: 10.1063/1.1566471]

I. INTRODUCTION

Metallic coatings, often composed of zinc or nickel, are used as protective coatings for corrosion-sensitive materials. There is also a rapidly growing interest in thin metallic films because of their use in microelectronic devices and magnetic multilayers. While protective coatings typically have thicknesses of the order of 100 μm, the films in microelectronic devices and magnetic multilayers have thicknesses down to a fraction of a micrometer. The stress level in these thin films exhibits a size effect, with thinner films generally having higher stress levels (see Ref. 1 for a review).

An important source of stress in thin films arises from the thermal mismatch between the film and the substrate. Experiments that reveal this, typically involve cooling, heating or an alternating sequence of cooling and heating, with the average stress in the film recorded by wafer curvature measurements[2,3] or by x-ray diffraction.[2,4,5] On cooling a film from an almost stress-free state at a relatively high temperature, the deformation is initially elastic, but as cooling proceeds plastic deformation eventually occurs. When the film is reheated, the stress level in the film at first reduces (in absolute value) elastically, with reverse plastic deformation subsequently occurring for a sufficiently large temperature change. Reverse plastic deformation occurs earlier and stress levels increase more rapidly for thinner films. These effects have been observed for fine-grained as well as coarse-grained films[3] and also in passivated films.[2,4]

This size effect is not captured by conventional continuum plasticity theories because they lack an internal length scale. Nonlocal phenomenological continuum plasticity theories have been proposed, e.g., Refs. 6–10, that can capture size effects within a phenomenological theory of plasticity. There have also been studies aimed at explaining the thin film size effect based on considerations of dislocation nucleation and motion. In addition to arguments that make reference to well-known concepts such as the Hall–Petch relation,[3] single dislocation models have been proposed for thin films. Freund[11] and Nix[12,13] have proposed a model based on the confined motion of a threading dislocation in a single crystal film, which suggests that the yield strength scales with the film thickness h as h^{-1}. Similar single dislocation arguments have been used for polycrystalline films in Refs. 14 and 15. Hartmaier *et al.*[16] have discussed the role of thickness on the possibility of generation of new dislocations.

Although single dislocation models may capture important aspects of the phenomenon, they ignore the stress evolution associated with interactions between multiple dislocations. Nix[12] conjectured that an array of misfit dislocations generated near the film/substrate interface could provide obstacles to the motion of additional, differently oriented, misfit dislocations, see also Ref. 5. A simple analysis of this mechanism gave very high strain hardening rates, substantially overestimating observed hardening rates.[12] In this article, we carry out a dislocation dynamics simulation of the evolution of plastic deformation in metal thin films subject to thermal loading. The analyses are carried out within a two-dimensional discrete dislocation plasticity framework, with all dislocation lines being parallel to each other. The elastic interactions between multiple dislocations, dislocation nucleation, glide and annihilation, as well as the roles of the stress-free surface and of the film-substrate interface are accounted for.

II. PROBLEM FORMULATION

We consider a single-crystalline film, of thickness h, perfectly bonded to an elastic half plane, as illustrated in Fig. 1. A two-dimensional, plane-strain study ($\varepsilon_{33}=0$) is carried out. The two-dimensional nature of the model is motivated by the consideration that it is the long straight edge part of threading dislocations that provides most of the plastic relax-
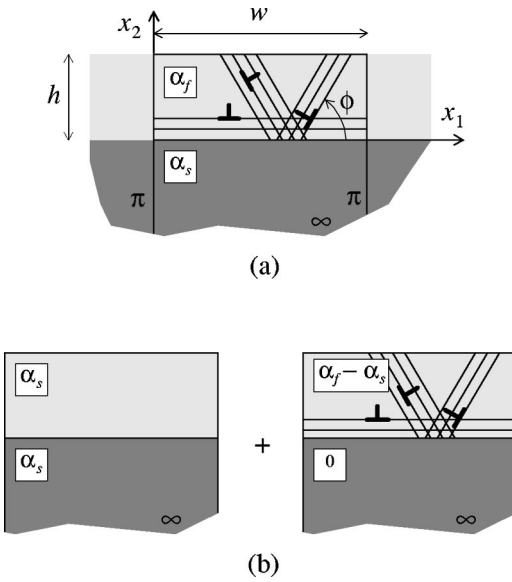
FIG. 1. (a) Geometry of the film-substrate problem studied in this article. (b) Decomposition of the unit-cell problem into a thermoelastic problem and a plastic relaxation problem. The solution of the latter part uses another decomposition, following Ref. 18.

ation. Three-dimensional effects such as line tension and the interaction between dislocation lines not parallel to existing misfit dislocation lines along the interface, as discussed in Ref. 12, are not accounted for. The substrate remains elastic, while the film can relax by dislocation activity on a set of discrete slip systems defined by the angle $\phi^{(\alpha)}$ relative to the interface, see Fig. 1(a). The dislocations are all of edge character with a Burgers vector in the x_1-x_2 plane of length b. Individual dislocations are modeled as singularities in an isotropic thermo-elastic continuum.

The boundary value problem is governed by the equilibrium and compatibility equations

$$\sigma_{ij,j}=0, \quad \varepsilon_{ij}=\tfrac{1}{2}(u_{i,j}+u_{j,i}), \tag{1}$$

where σ_{ij} denotes the stresses, ε_{ij} the strains and u_i the displacements; $(\ )_{,i}$ denotes partial differentiation with respect to x_i.

The constitutive relation is specified by

$$\varepsilon_{ij}=\frac{1+\nu}{E}\left(\sigma_{ij}-\frac{\nu}{1+\nu}\delta_{ij}\sigma_{kk}\right)+\alpha\Delta T\delta_{ij}. \tag{2}$$

Here, ΔT is the temperature change from the undeformed state. The linear thermal expansion coefficient α for the film is denoted by α_f and that for the substrate by α_s; Young's modulus E and Poisson's ratio ν are taken to be identical for the film and the substrate. In Ref. 17 it was found that elastic property differences did not qualitatively affect the predictions; quantitatively: even a factor of 2 difference in E changed predictions by only a few percent. The values of $E=70$ GPa and $\nu=0.33$ used in the calculations are representative of aluminum.

To implement the boundary conditions, the problem is decomposed in two linearly additive parts as illustrated in Fig. 1(b). One part treats the unconstrained thermal expansion of the film and substrate as if they have the same thermal expansion coefficient, $\alpha_f=\alpha_s$. The solution to this problem is

$$\varepsilon_{ij}^{th}=(1+\nu)\alpha_s\Delta T\delta_{ij}, \quad \sigma_{ij}^{th}=0 \quad (i,j=1,2) \tag{3}$$

for both film and substrate (the factor $1+\nu$ is due to the plane strain constraint in the x_3 direction). Since the stresses vanish everywhere, this part of the solution does not interact with the dislocations.

The other part of the solution, which is denoted by $(\ )'$ and pertains to the problem sketched in Fig. 1(b), describes the stress which builds up in the film due to the thermal mismatch between the film and the substrate, and accounts for the presence of the dislocations. This problem pertains to a film with a thermal expansion coefficient $\alpha=\alpha_f-\alpha_s$ on a substrate that does not undergo thermal expansion. The solution to the full problem is

$$u_i=u_i^{th}+u_i', \quad \varepsilon_{ij}=\varepsilon_{ij}^{th}+\varepsilon_{ij}', \quad \sigma_{ij}=\sigma_{ij}^{th}+\sigma_{ij}'. \tag{4}$$

With plasticity arising from the collective motion of discrete dislocations, the $(\ )'$ solution is not independent of x_1. As shown in Fig. 1(a), a unit cell is introduced in order to reduce the computation to one over a finite region. The film-substrate system is taken to be periodic in the x_1 direction with period w. The boundary conditions on the unit cell consist of the stress-free surface conditions

$$\sigma_{12}'(x_1,h)=\sigma_{22}'(x_1,h)=0 \tag{5}$$

and the periodicity conditions

$$u_i'(0,x_2)=u_i'(w,x_2), \tag{6}$$

while traction continuity implies continuity of σ_{12}' and σ_{11}' at the cell boundaries $x_2=0$ and $x_2=w$. The $(\ )'$ fields are governed by Eqs. (1) and (2) with the appropriate substitutions for α according to Fig. 1(b). In the absence of dislocations, the solution is

$$\varepsilon_{ij}'=0, \quad \sigma_{11}'=-\frac{(\alpha_f-\alpha_s)E\Delta T}{(1-\nu)},$$
$$\sigma_{ij}'=0 \quad \text{otherwise} \quad (i,j=1,2) \tag{7}$$

for the film and $\varepsilon_{ij}'=\sigma_{11}'=0$ everywhere in the substrate. The solution (7) can be interpreted as resulting from the film freely expanding by $(\varepsilon_{11}^{th})_f=(1+\nu)(\alpha_f-\alpha_s)\Delta T$ and subsequently being compressed by a stress σ_{11}' to remove the expansion so that the film fits on the undeformed substrate.

In the presence of dislocations, the governing equations, subject to Eqs. (5) and (6), are solved by decomposing the $(\ )'$ field quantities into two additive parts, as described in Ref. 18, so that the stress, strain and displacement fields in the film are given by

$$u_i'=\tilde{u}_i+\hat{u}_i, \quad \varepsilon_{ij}'=\tilde{\varepsilon}_{ij}+\hat{\varepsilon}_{ij}, \quad \sigma_{ij}'=\tilde{\sigma}_{ij}+\hat{\sigma}_{ij}. \tag{8}$$

Here, the $(\ )$ fields are the superpositions of the fields of individual dislocations in infinite space, e.g.,

$$\tilde{\sigma}_{ij}=\sum_I \sigma_{ij}^{(I)}$$

(the superscript (I) denotes the Ith dislocation), and are singular at the positions of the dislocations. The $(\hat{\ })$ fields in Eq. (8) are image fields that are superimposed on the individual

dislocation fields so that the boundary conditions on the unit cell are satisfied. These fields are smooth and their solution is obtained by a finite element method. The infinite space ($\sim$) fields are constructed in such a way that they reflect the periodicity in the problem, i.e., the field corresponding to each dislocation in the cell is the field, with periodicity w, due to this dislocation and all its replicas in the other cells making up the film. The closed-form expressions for these fields are given in Ref. 19. The use of periodic discrete dislocation fields avoids the possibility of artificial dislocation patterning that may be induced when using a cutoff distance.[20]

Special attention is needed for dislocations that glide out of the film. They leave the film, but they cannot be removed from the set of dislocations in the calculation because they contribute to a slip displacement and to the resulting step at the free surface. This is accounted for by virtually extending the slip planes above the film and positioning a dislocation at a distance h above the free surface, i.e., at $x_2 = 2h$, once it leaves the film. This virtual dislocation produces stresses $\tilde{\sigma}_{12}$ and $\tilde{\sigma}_{22}$ on the stress-free surface (even though it is outside the film). These stresses are corrected by the ($\wedge$) fields. The virtual dislocations at $x_2 = 2h$ are sufficiently far away from the surface that the finite element solution can accurately describe the necessary correction.

Initially, the film-substrate system is at a high temperature and stress free. At each step of the simulation a temperature increment $\Delta T = \dot{T}\Delta t$ is prescribed and the boundary value problem is solved for all field quantities in the cell. For each time step, the dislocation structure is updated and then the updated solution for all field quantities is obtained as described above. As suggested by Kubin et al.,[21] the following dislocation mechanisms are accounted for through constitutive rules: (i) dislocation glide; (ii) dislocation generation and (iii) annihilation; (iv) pinning at obstacles. All of these are governed by the Peach–Koehler force, which is computed as

$$f^{(I)} = n_i^{(I)}\left(\hat{\sigma}_{ij} + \sum_{J \neq I} \sigma_{ij}^{(J)} \right) b_j^{(I)}$$

taking advantage of the fact that $\sigma_{ij}^{\text{th}} = 0$ according to Eq. (3).

Dislocation glide is taken to be drag controlled so that the velocity of dislocation I is directly proportional to the Peach–Koehler force, $f^{(I)} = Bv^{(I)}$, with B the drag coefficient, which is taken to have the value $B = 10^{-4}$ Pa s. Annihilation of two dislocations with opposite Burgers vector occurs when they approach each other within an annihilation distance $L_e = 6b$. Generation of new dislocations is incorporated through a distribution of Frank–Read sources. In two dimensions, these are point sources which generate a dipole when the Peach–Koehler force on the source exceeds a critical value $\tau_{\text{nuc}}b$ during a time span $t_{\text{nuc}} = 10$ ns. The sign of the dipole is determined by the direction of the force. The distance between the two dislocations, L_{nuc}, is set so that they will not immediately collapse and annihilate under an applied shear stress τ_{nuc}, i.e.,

$$L_{\text{nuc}} = \frac{\mu}{2\pi(1-\nu)} \frac{b}{\tau_{\text{nuc}}} \qquad (9)$$

with $\mu = E/2/(1+\nu)$ the shear modulus. A distribution of point obstacles, which are intended to mimic small precipitates or forest dislocations, is also introduced. Dislocations get pinned at such obstacles and are released once the Peach–Koehler force attains the obstacle strength $b\tau_{\text{obs}}$.

III. RESULTS

The objective of the simulations is to gain insight into the thickness-dependent response of thin films. We consider representative values of the material parameters. The Burgers vector of the film material is taken to be $b = 0.25$ nm. The linear coefficient of thermal expansion is taken to be representative of silicon for the substrate ($\alpha_s = 4.2 \times 10^{-6}$/K) and of aluminum for the film ($\alpha_f = 23.2 \times 10^{-6}$/K). Results are presented for values of the film thickness, h, ranging from 0.25 to 1 μm. In all calculations, the width of the periodic cell is taken to be $w = 2$ μm. The potentially active slip planes for each slip system are spaced at $d = 100b$, so that there are $n = (w/d)\sin\phi$ slip planes with orientation ϕ inside the cell.

In all the simulations the density of Frank–Read sources randomly distributed on the slip planes is $\rho_{\text{nuc}} = 60/\mu\text{m}^2$. This implies that there are 120 sources per micrometer of film thickness in the cell, which means that not all slip planes are necessarily active. On the other hand, for the thickest films considered, $h = 1$ μm, there are as many as four sources per slip plane. The strength of the sources is taken randomly from a Gaussian distribution with mean strength $\bar{\tau}_{\text{nuc}} = 25$ MPa and standard deviation of 5 MPa. With the chosen material properties, the mean nucleation distance from Eq. (9) is $L_{\text{nuc}} = 0.0625$ μm, which is 1/4 of the smallest film thickness $h = 0.25$ μm, and, more importantly, only 1/8 of the shortest slip plane length $h/\sin 60°$. However, since the strengths are taken from a Gaussian distribution, values of L_{nuc} can deviate significantly from the average. In the distributions used in the calculations here, the smallest value of τ_{nuc} is 10 MPa, which corresponds to $L_{\text{nuc}} = 0.156$ μm. All sources are displaced by at least the distance $L_{\text{nuc}}\sin\phi$ from the top or bottom of the film, in order that both dislocations in a nucleated dipole are contained in the film. Whenever obstacles are considered, their density is taken to be the same as the source density and their strength is specified as $\tau_{\text{obs}} = 150$ MPa.

In order to limit the computational time, the cooling rate is specified as $\dot{T} = 40 \times 10^6$ K/s and the total temperature decrease is 200 K, which is smaller than usual in experiments. A small time step is required to accurately resolve the dislocation dynamics. Numerical experimentation showed that with the parameters used here, a time step Δt no larger than 0.05 ns is needed mainly to capture the formation of dislocation junctions (dipoles) near the intersection of slip planes.

The finite element mesh used to solve for the ( ) fields depends on the thickness of the film. In all cases, four-node elements are used which are nearly square in the film and which gradually elongate inside the substrate with increasing depth. For the thinnest films considered, $h = 0.25$ μm, we have used ten elements through the film thickness. Numerical tests have shown that this gives sufficient resolution over

the top surface to satisfy the stress-free condition with sufficient accuracy.

Each simulation starts with a dislocation-free film, so that when cooling begins, the response is initially elastic. As the temperature decreases, a uniform tensile stress builds up in the film. When the resolved shear stress on a slip system reaches the critical strength of the weakest point source, the source generates a dislocation dipole. One of the dipole dislocations glides in the direction of the free surface and the other glides toward the interface where it gets pinned. It is this movement which provides the mechanism of plastic relaxation of the thermal stress. As cooling proceeds, many other dislocations are nucleated. Because of the stress fields associated with the individual dislocations in the film, the Peach–Koehler force at a source can become large enough to induce a nucleation event, even if the average stress in the film is not high enough to activate the source.

A. Size effect

We first present results for three cases that differ in the film thickness only: $h = 1$, 0.5, and 0.25 μm. The film material contains three slip systems, with slip plane orientations: $\phi^{(1)} = 0°$; $\phi^{(2)} = 60°$; $\phi^{(3)} = 120°$. The three slip systems mimic in two dimensions the redundancy of the 12 available slip systems in fcc crystals.

Figure 2 shows the distribution of the dislocations and the in-plane stress σ_{11} at the end of the cooling process. The stress is normalized by the elastic stress

$$\sigma_n = -\frac{(\alpha_f - \alpha_s)E\Delta T}{(1-\nu)}, \tag{10}$$

which would be present in the film if plastic relaxation had not occurred, see Eq. (7). With the parameter values here, $\sigma_n = 397$ MPa. For each film thickness, a single unit cell of the film as well as the top of the substrate is shown. For the chosen thermal expansion coefficients and with $\Delta T < 0$, the film is in a state of tension, $\sigma_n > 0$. The compressive stress in the substrate is very low on average, because of its large thickness, except in a thin layer directly below the interface which is affected by the dislocations in the film near the interface. Indeed, a relatively large number of dislocations are piled up in the film against the interface because the interface is modeled as being impenetrable. Due to this local high dislocation density, a boundary layer forms with a much higher in-plane stress than in the rest of the film.

A boundary layer is also seen in the dislocation density profiles $\rho(x_2)$ across the film, shown in Fig. 3. The dislocation density plotted is the average dislocation density in a strip of height λ, averaged in the x_i-direction. Making use of periodicity, this quantity is computed as

$$\rho(x_2) = \frac{1}{bw\lambda} \sum_I b^{(I)},$$

$$\forall I \text{ such that } x_2 - \lambda/2 < x_2^{(I)} < x_2 + \lambda/2. \tag{11}$$

Using a strip height of $\lambda = 0.025$ μm, the profiles in Fig. 3 show that there is a distinct peak in the bottom strip which is roughly the same for all three thicknesses. The thickness of the highly stressed boundary layer is less than 0.025 μm
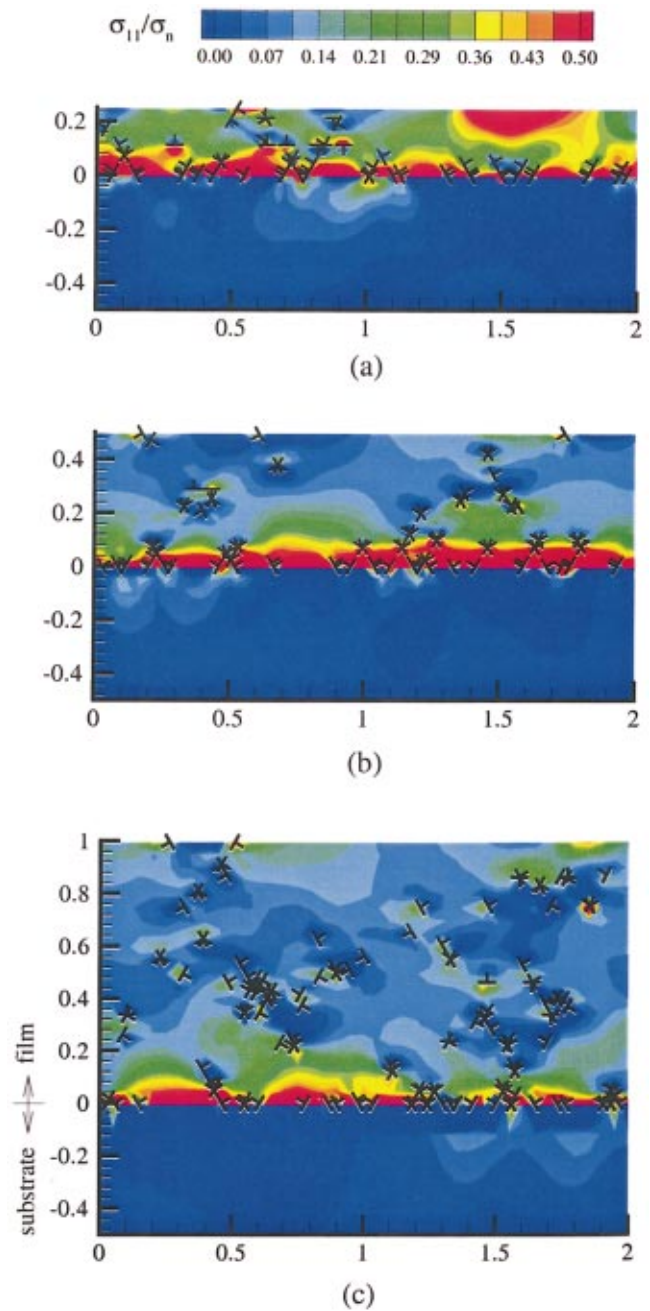

FIG. 2. (Color) Distribution of σ_{11}, normalized by σ_n defined in Eq. (10), and the dislocation distribution after cooling by 200 K for three values of film thickness: (a) $h = 0.25$ μm, (b) $h = 0.5$ μm and (c) $h = 1$ μm. The films have three slip systems with slip plane orientations specified by $\phi^{(1)} = 0°$, $\phi^{(2)} = 60°$, and $\phi^{(3)} = 120°$ (see Fig. 1).

$= 100b$. The dislocation density in the rest of the film, where the tensile stress has been relaxed (Fig. 2), is at least a factor 4 lower and also appears to be about the same for the three cases.

Examining the near-interface dislocations shown in Fig. 2 reveals that they are either positive dislocations on the $\phi^{(2)} = 60°$ slip planes or negative dislocations on the $\phi^{(3)} = 120°$ slip planes. In both cases the horizontal component of the Burgers vector is in the positive x_1 direction. Neglecting the low density of dislocations in the rest of the film, the classical idealized picture emerges of a film that is relaxed by
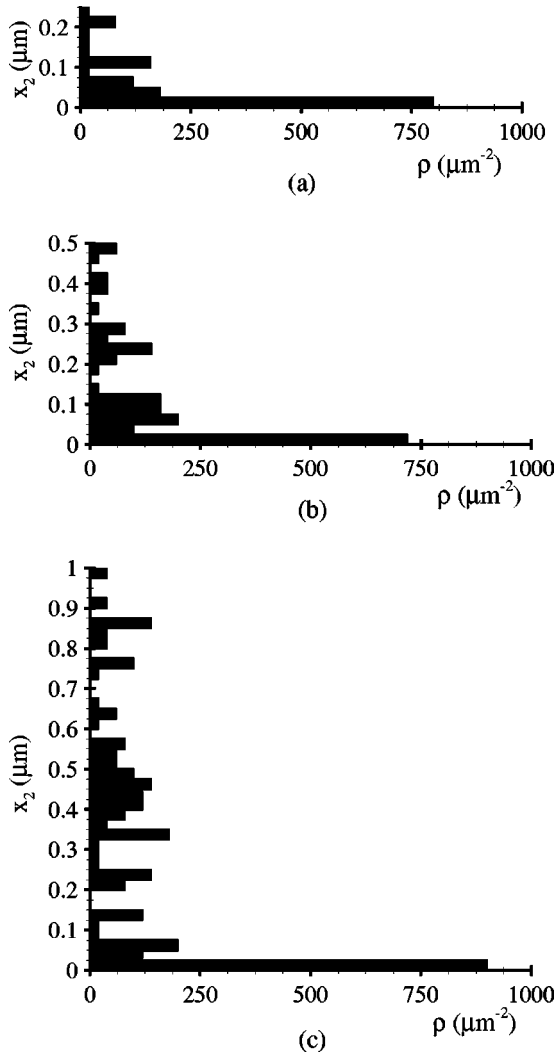
FIG. 3. Dislocation density profile across the film thickness for the films in Fig. 2. (a) $h=0.25$ μm, (b) $h=0.5$ μm and (c) $h=1$ μm.
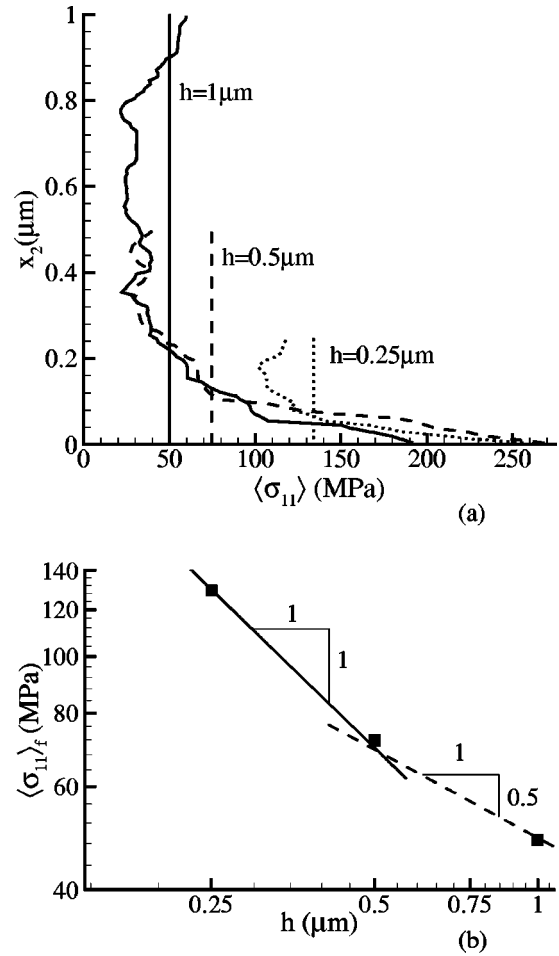

FIG. 4. (a) Profiles $\langle \sigma_{11} \rangle (x_2)$ of the in-plane stress in the films in Fig. 2 averaged in the x_1 direction. The vertical lines show the total film averages, $\langle \sigma_{11} \rangle_f$. (b) Average film stress vs film thickness h. The straight lines are fits to a power law of the form $\langle \sigma_{11} \rangle_f \propto h^{-p}$, giving $p \approx 1$ for the thinnest two films and $p \approx 1/2$ for the thicker ones.

a distribution along the interface of misfit dislocations with Burgers vector $b|\cos \phi|$ in the x_1 direction. Full relaxation of the film would require that the thermal strain $(\varepsilon_{11}^{th})_f = (1 + \nu)(\alpha_f - \alpha_s)\Delta T$ is entirely accommodated by such misfit dislocations. The dislocation density in a strip of height λ needed for this is given by

$$\rho = \frac{(1+\nu)(\alpha_f - \alpha_s)\Delta T}{\lambda b \cos \phi}. \tag{12}$$

For $\lambda = 0.025$ μm, this expression gives a density $\rho = 1.6 \times 10^3$ μm^{-2}. The dislocation density in the bottom strip λ of Fig. 3 is around 800 μm^{-2}. This is significantly less than the necessary dislocation density for a completely stress-free film. Thus we expect that there is a significant stress component σ_{11} left in the film.

Figure 2 gives insight into the nature of this stress state. An additional perspective is given by the x_1-averaged σ_{11} profiles in Fig. 4(a) for the three film thicknesses considered at $\Delta T = 200$ K. The x_1-averaged stresses, $\langle \sigma_{11} \rangle (x_2)$, are computed in a strip-wise fashion as in Eq. (11), i.e.,

$$\langle \sigma_{11} \rangle (x_2) = \frac{1}{w \lambda} \int_{x_2 - \lambda/2}^{x_2 + \lambda/2} \int_0^w \sigma_{11}(x_1, z_2) dx_1 dz_2. \tag{13}$$

The integral is evaluated using 5×5 trapezoidal quadrature in each strip with height λ of a finite element. A value of $\lambda = 0.0167$ μm was found to give well-converged results of $\langle \sigma_{11} \rangle (x_2)$. Also shown in Fig. 4(a) are the average stresses in the film: $\langle \sigma_{11} \rangle_f = 50$, 70, and 130 MPa for $h=1$, 0.5, and 0.25 μm, respectively (with $\langle \rangle_f$ denoting the film average of a quantity). The profiles clearly show the presence of highly stressed boundary layers and also illustate the variation in boundary layer thickness with film thickness. For the two thickest films, the boundary layer thicknesses are nearly the same, but the boundary layer in the thinnest film is significantly thinner. It is also of importance to note that the stress level in the core of the $h=0.25$ μm film is higher than for the other two films. It is primarily this lack of relaxation in the core that causes the $h=0.25$ μm film to have such a high average stress.

Average stress, $\langle \sigma_{11} \rangle_f$, versus film thickness h is shown in Fig. 4(b) to illustrate the scaling with film thickness. The thicker two films suggest a Hall–Petch-like $h^{-1/2}$ scaling. The data for the thinnest two films are consistent with the
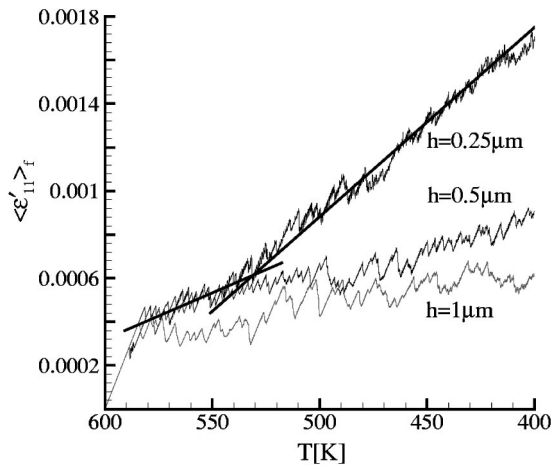
J. Appl. Phys., Vol. 93, No. 10, 15 May 2003

Nicola, Van der Giessen, and Needleman   5925

FIG. 5. Curves of $\langle \varepsilon'_{11} \rangle_f$ vs imposed temperature for three values of film thickness: $h = 0.25$ μm, $h = 0.5$ μm and $h = 1$ μm (see Figs. 2 and 3).

h^{-1} scaling found by Freund[11] and Nix[12] on the basis of energy considerations. Although data from three points is not conclusive, we believe that the dichotomy in scaling is due to a change in hardening mechanism for the thinnest film, as will be discussed in detail in Sec. III C. We note that the average film stresses are not sensitive to the source distribution; other realizations give results that only differ by a few percent.

While we have focused until now on the stress states at the end of the cooling process, the full history is shown in Fig. 5. Rather than stress, however, Fig. 5 shows the evolution of $\langle \varepsilon'_{11} \rangle_f$ as a function of the temperature reduction. The value of $\langle \varepsilon'_{11} \rangle_f$ represents the average lattice strain in the film due to the thermal mismatch with the substrate. Adding ε^{th}_{11} to it, Eq. (3), gives the quantity which is usually measured experimentally by x-ray diffraction.[4,22] From $\langle \varepsilon'_{11} \rangle_f$ and the corresponding $\langle \varepsilon'_{22} \rangle_f$, the average stress $\langle \sigma'_{11} \rangle_f$ can be directly computed from Hooke's law, Eq. (2), with $\alpha = 0$. Since $\sigma^{th}_{ij} = 0$, Eq. (3), this immediately gives the total average film stress $\langle \sigma_{11} \rangle_f$, cf. Eq. (4). Thus, plots of the evolution of $\langle \varepsilon'_{11} \rangle_f$ give insight into the average stress development in the film.

The curves in Fig. 5 exhibit a distinct size effect on the hardening, with thinner films being harder. The yield point, which corresponds to a yield stress of about 30 MPa, does not exhibit a size effect, as the initiation of plastic deformation is controlled by the statistical distribution of source strengths. Prior to the first nucleation event, the stress in the film is uniform, so that the first occurrence is determined by the weakest source. Since the source strengths are chosen randomly from a Gaussian distribution around a certain value, and since the specific values of source strength are different for different films, plastic deformation starts first in the film that contains the weakest source. For the cases shown in Fig. 5 this happened to be the thinnest film, where the minimum nucleation strength, out of the average of $\bar{\tau}_{nuc} = 25$ MPa, is $\tau_{nuc} = 10$ MPa.

Hardening, on the other hand, is a collective effect of the nucleation, glide and annihilation of a large number of dislocations. Statistical effects are therefore smaller. The hard-

ening rate averaged over a temperature drop of $\Delta T = 185$ K from the onset of yield, $\Delta \langle \sigma_{11} \rangle_f / \varepsilon^{th}_{11}$ is 18, 39, and 97 GPa for $h = 1$, 0.5, and 0.25 μm, respectively. To check the sensitivity of the yield stress and hardening rate to the value of τ_{nuc}, the calculations were repeated with the same source distributions but with the value of τ_{nuc} at each source multiplied by a factor of 2. The values of the yield stress for each of the three films doubled, while the values of the hardening rate remained essentially unchanged.

Calculations were repeated with all parameters fixed except that a random array of point obstacles was added with a density of $60/\mu m^2$. Figure 6 shows that the dislocation density in the core region is higher with obstacles than without obstacles (especially for the thickest film), since the obstacles tend to prevent dislocations from leaving the film at the free surface. In fact, numerous dislocation dipoles form at slip plane intersections, leading to a harder core region than without obstacles which gives rise to the increased hardening rate seen in Fig. 7 compared with that in Fig. 5.

B. Effect of slip plane orientation

In order to investigate the influence of slip plane orientation, the simulations presented in the previous section have repeated with the crystal rotated by $\pm 30°$, so that $\phi^{(1)} = 30°$; $\phi^{(2)} = 90°$; $\phi^{(3)} = 150°$ The source density is the same as before, but the source positions and strengths are different; there are no obstacles. Slip systems 2 and 3 are the most active ones, because the resolved shear stress $\tau = -\sigma_{11}/2 \sin 2\phi$, caused by a nominal tensile stress σ_{11}, is largest in absolute value. In fact, the Schmid factor $|\sin 2\phi|$ is the same as for the $\pm 60°$ slip systems in the original orientation. This explains that the onset of yield (Fig. 8) is roughly the same as for the original crystal orientation (Fig. 5).

The hardening in the film is reduced however, i.e., the stress is more relaxed in the rotated orientation for all film thicknesses, cf. Fig. 8 with Fig. 5. One explanation for this is that fewer dislocations are needed to relax the film in the rotated orientation: according to Eq. (12) with $\phi = \phi^{(1)} = 30°$, a dislocation density $\rho = 900$ μm^{-2} is needed in the height $\lambda = 0.025$ μm for complete relaxation. The dislocation density found near the interface is around 600 μm^{-2} for all three thicknesses. This is a higher percentage (67%) than for the previous orientation (50%), which is consistent with the film being more relaxed.

The dislocation distribution along with the boundary layer that forms in the thinnest film with orientation $\phi^{(1)} = 30°$ is seen in Fig. 9(a). Profiles of x_1-averaged stresses for all three thicknesses reveal that the boundary layers have the same thickness, which is slightly smaller than that seen in Fig. 4(a) for the original orientation. A second difference is that the core region of the films is less stressed. The two effects explain the lower hardening in Fig. 8.

To investigate the orientation dependence further, simulations were carried out in single slip with slip plane orientations of $\phi = 15°$, $30°$, $60°$, and $75°$. In single slip, dislocations do not form junctions, so that the time step can be increased by an order of magnitude without losing accuracy. Figure 10 shows that the hardening rate increases with in-
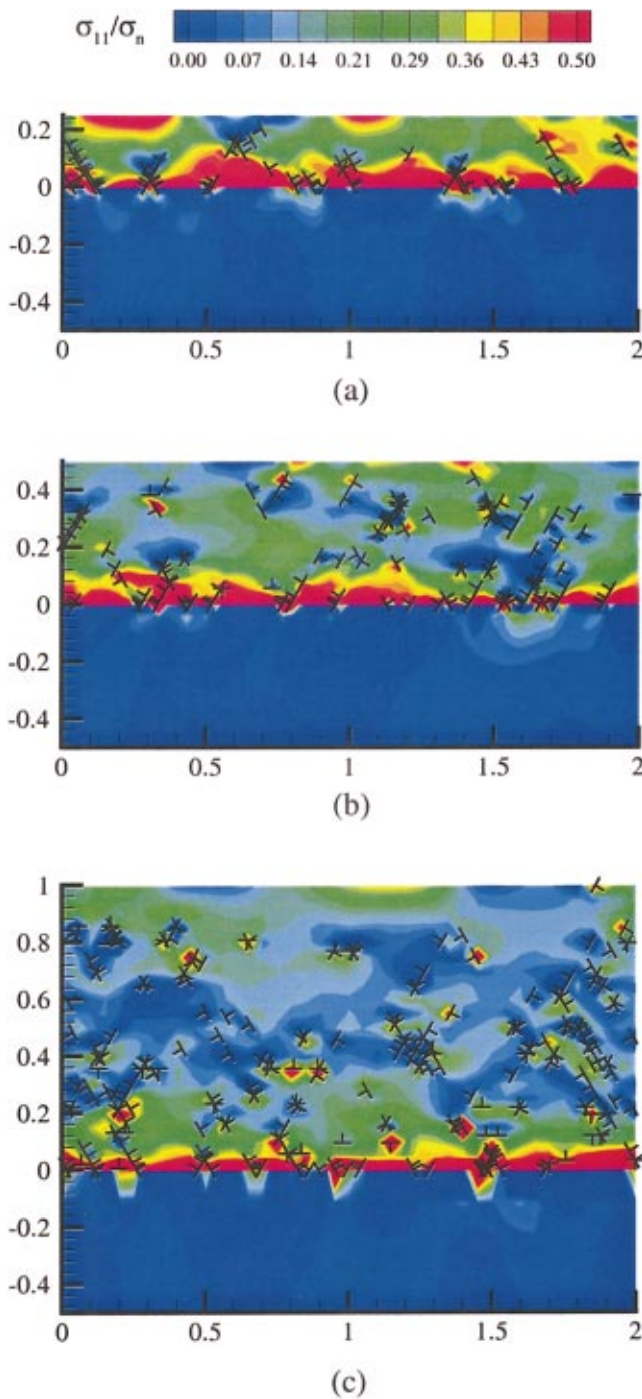
(a)

(b)

(c)

FIG. 6. (Color) Distribution of σ_{11}, normalized by σ_n defined in Eq. (10), and the dislocation distribution after cooling by 200 K for three values of film thickness: (a) $h=0.25$ μm, (b) $h=0.5$ μm and (c) $h=1$ μm with a prescribed distribution of dislocation obstacles. The slip plane orientation is the same as in Fig. 2.

creasing ϕ. This is mainly due to a combination of the orientation dependence of the Schmid factor and of the slip plane length $h/\sin\phi$. Also, we see that plastic flow occurs earlier for slip plane orientations of 30° and 60° than for those of 15° and 75°, because the resolved shear stress τ is larger for the 30° and 60° orientations.

C. Origin of hardening

Examination of the average strain-temperature curves in Figs. 5 and 8 indicates that there is a more or less pro-
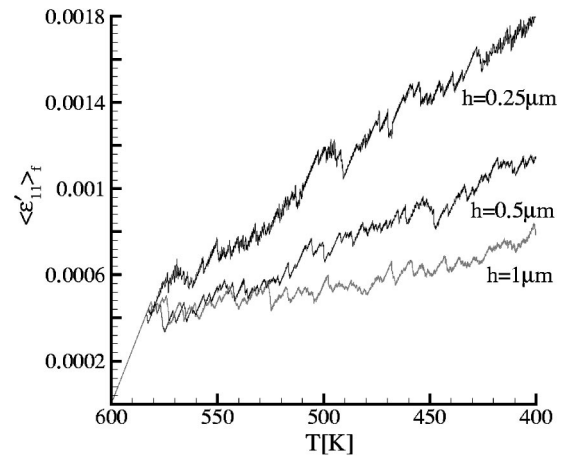

FIG. 7. Curves of $\langle\varepsilon'_{11}\rangle_f$ vs imposed temperature for three values of film thickness: $h=0.25$ μm, $h=0.5$ μm and $h=1$ μm for the calculation in Fig. 6 with a prescribed distribution of dislocation obstacles.

nounced kink in the average slope after the onset of plasticity as exemplified in Fig. 5. These kinks reflect a change in the hardening rate in the plastic regime. For the smallest thickness, $h=0.25$ μm, the kink is most clearly visible; also for the thickest film, $h=1$ μm, a kink can be observed but it occurs at a later stage. Moreover, we observe that the hardening in the second part of the curve increases with the slip plane angle, as seen by comparing Figs. 5 and 8. A significant increase in hardening has been noted experimentally by Leung et al.[2] in various types of films, and can also be seen in the experimental results in Ref. 4. The strongest effect is always seen, as here, for very thin films. The effect is not found by Leung et al.[2] for passivated films, which has led them to suggest that the effect is due to additional relaxation by surface diffusion at higher temperature. However, the experimental results in Ref. 4 also show a two-stage hardening effect for very thin ($h=0.3$ μm) passivated films. In our calculations there is no diffusion, and therefore it is interesting to explore the origin of the kink in the simulations.

One possible cause is a sudden increase in dislocation density, leading to an increase in the number of dislocation junctions and therefore to an increase in hardening. However, since the kink is present in multiple slip as well as in single slip (no junctions), Fig. 10 and Fig. 5, this is excluded. Another possible cause is an abrupt reduction of the rate of dislocations nucleated. This is what happens in our calcula-
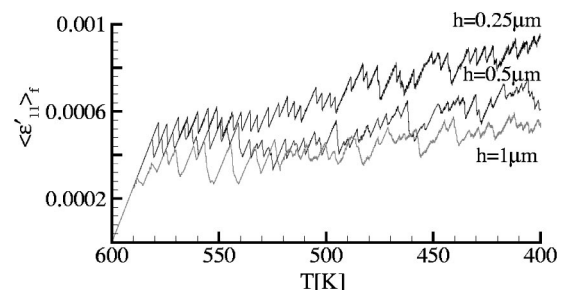

FIG. 8. Curves of $\langle\varepsilon'_{11}\rangle_f$ vs imposed temperature for three values of film thickness: $h=0.25$ μm, $h=0.5$ μm and $h=1$ μm. The films contain three slip systems with slip plane orientations $\phi^{(1)}=30°$, $\phi^{(2)}=90°$, and $\phi^{(3)}=150°$.

(a)

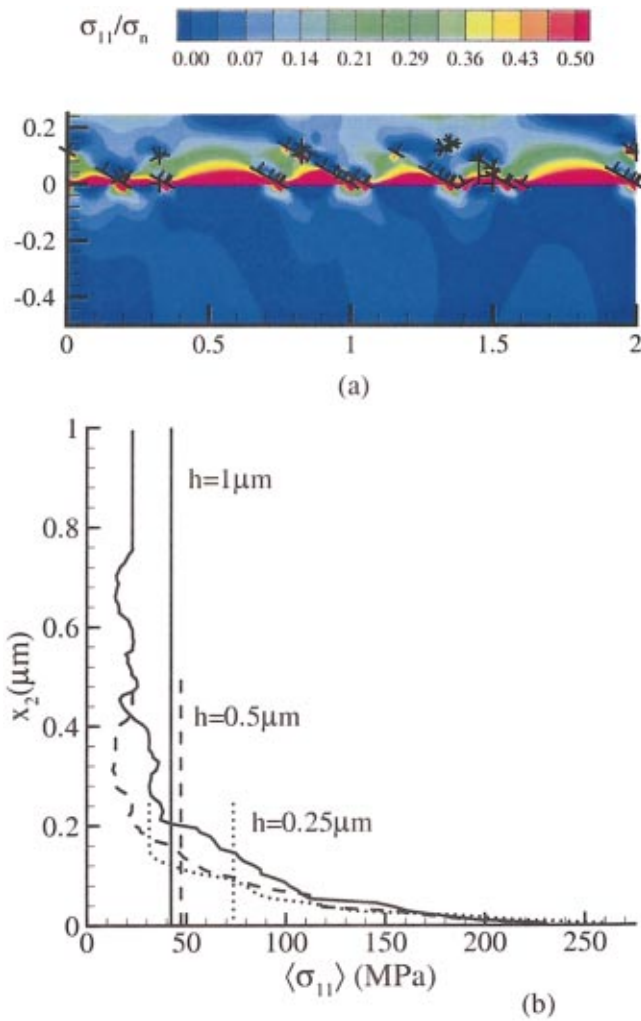FIG. 11. (Color) Distribution of resolved shear stress on the slip plane $\phi^{(2)}=60°$, τ_{60} and the dislocation distribution at final temperature for the film in Fig. 2(a). The point sources on this slip system are shown as circles.

(b)

FIG. 9. (Color) Internal stress states for the films in Fig. 8 after cooling by 200 K. (a) Contours of σ_{11}, normalized by σ_n defined in Eq. (10), and the dislocation distribution for $h=0.25$ μm. (b) Profiles $\langle\sigma_{11}\rangle(x_2)$ of the in-plane stress in all films with this orientation. The vertical lines show the total film averages, $\langle\sigma_{11}\rangle_f$.
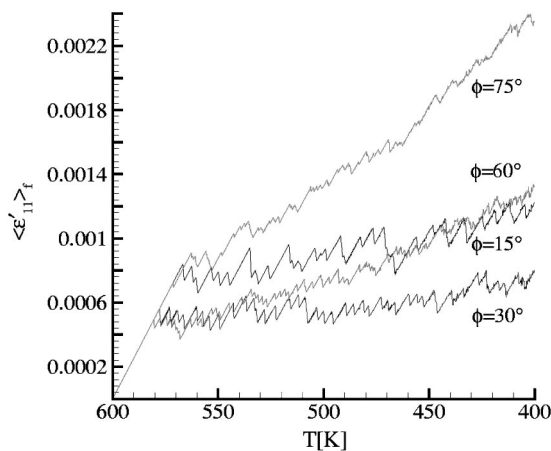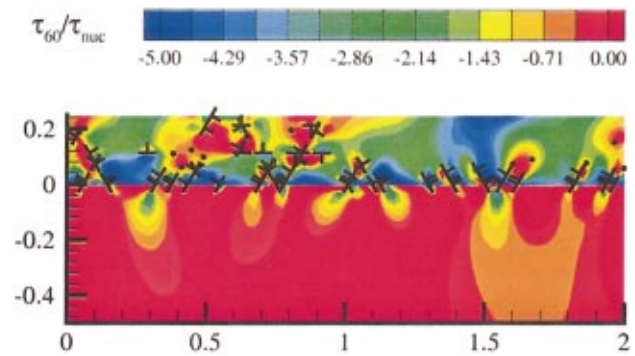

FIG. 10. Curves of $\langle\varepsilon'_{11}\rangle_f$ vs imposed temperature for films with a single slip system having the slip planes oriented at $\phi^{(1)}=15°$, $\phi^{(2)}=30°$, $\phi^{(3)}=60°$ and $\phi^{(1)}=75°$. All films have thickness $h=0.25$ μm.

tions, with the reduction in nucleation rate arising from the back stress generated by the dislocations in the boundary layer adjacent to the interface. For each source, nucleation first occurs when the resolved shear stress reaches τ_{nuc}. The stress field of the dipole generated by this source shields the source from further nucleation. The back stress at the source reduces as the dipole spreads, with the least effect occurring when one of the dislocations has left the film through the free surface and the other is blocked near the interface. In very thin films the back stress in this configuration is still high enough to have a significant effect at the source. During the first stage of the cooling process, other sources in the film will be activated before the back stress at previously activated sources has been overcome by the applied stress. This gives rise to the initial hardening rate. At some stage of the deformation history, all sources have been activated and collectively they have produced back stress throughout the film. Subsequently, the only way in which sources can be activated is by overcoming the back stress through further straining of the film. Thus, nucleation is delayed, which gives rise to additional hardening in the $\langle\varepsilon'_{11}\rangle_f-\Delta T$ curves.

To support this explanation, Fig. 11 shows the distribution of the resolved shear stress τ for the film with $h=0.25$ μm on slip system $\phi^{(2)}=60°$ at the same time as in Fig. 2(a). Also shown are all sources that are present on these slip planes to demonstrate that they are all in regions with relatively low stress due to the back stresses caused by the dislocations piled up against the interface. As the thickness of the film increases, the back stress at a source caused by the dislocation pileups at the film-substrate interface will, on average, be lower because of the larger distance between the pileup and the source. Hence, for thicker films, the kink in hardening is delayed and is less intense. This is confirmed by the results in Figs. 5 and 8.

The presence of the back stress is expected to give an important contribution to the response when the temperature change is reversed. This is verified for the thinnest film, by reheating from the final temperature of $T=400$ K reached previously. As seen in Fig. 12, reverse plasticity occurs almost immediately after temperature reversal for $h=0.25$ μm. Without the presence of the long-range back stresses, elastic unloading would occur over a larger interval.
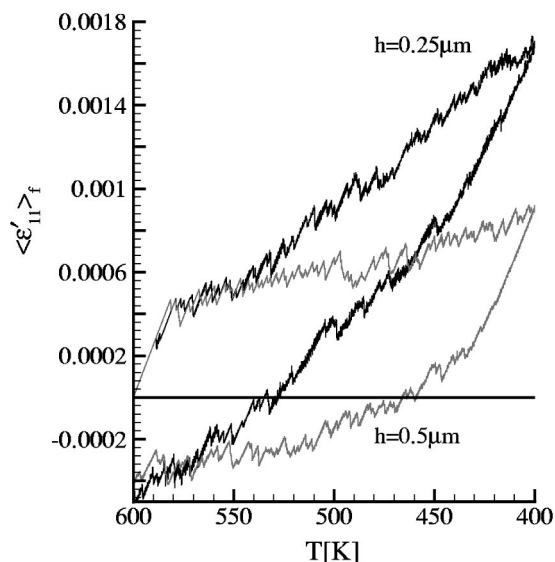
FIG. 12. Curves of $\langle\varepsilon'_{11}\rangle_f$ vs imposed temperature for a thermal cycle between 600 and 400 K for films of thickness $h=0.25$ μm and $h=0.5$ μm.

It should also be noted that the resolved shear stress distribution in Fig. 11 does not exhibit the same clear boundary layer as does the distribution of σ_{11} in Fig. 2(a). This suggests a limitation to the classical picture of misfit dislocations with Burgers vector parallel to the interface. The piled-up dislocations on the inclined slip planes do not neatly combine to such misfit dislocations: on average they do, but not point wise along the interface. In fact, closer examination of the dislocation structure shown in Fig. 5(a) shows the presence of pileups of two or three dislocations on the same slip plane. As there are no dislocations on a nearby inclined slip plane to cancel the resulting long-range back stress, the back stress remains effective for blocking nucleation on the same slip plane.

IV. CONCLUSIONS

Discrete dislocation analyses have been carried out of the stress evolution in single crystal films arising from the thermal mismatch between the film and its substrate. Attention was confined to plane strain, with the substrate remaining elastic and any effect of elastic mismatch between the film and substrate neglected. The film is initially dislocation free and the dislocations in the film, which are all of edge character, nucleate from Frank–Read sources on a specified set of slip planes. At the start of a calculation, the film-substrate system is stress free and the deformation arises from a prescribed temperature history. The results exhibit the following trends:

(i) The stress evolution and the hardening show a clear dependence on film thickness for the thicknesses analyzed which range from 0.25 to 1 μm.

(ii) The effect of film thickness is mainly due to the formation of a hard boundary layer at the film-substrate interface. The width of the boundary layer, which arises from dislocation pileups at the interface, does not scale with the film thickness.

(iii) The boundary layer width depends on the orientation of the slip systems in the film.

(iv) Below a certain film thickness, an additional contribution to hardening arises from a reduction in dislocation nucleation caused by the back stress associated with the dislocation pileups at the film-substrate interface. This reduction in the rate of dislocation nucleation can occur abruptly and lead to a two-stage hardening behavior as seen experimentally.

(v) In very thin films all the available dislocation sources are affected by the back stress early in the stress relaxation process. Further nucleation is suppressed until the back stress at the sources is overcome by additional straining of the film. The absence of dislocations that can eliminate the long-range back stress is related to the limited availability of sources.

[1] E. Arzt, Acta Mater. **16**, 5611 (1998).
[2] O. S. Leung, A. Munkholm, S. Brennan, and W. D. Nix, J. Appl. Phys. **88**, 1389 (2000).
[3] R. Venkatraman and J. C. Bravman, J. Mater. Res. **7**, 2040 (1992).
[4] S. P. Baker, A. Kretschmann, and E. Arzt, Acta Mater. **49**, 2145 (2001).
[5] M. Hommel and O. Kraft, Acta Mater. **49**, 3935 (2001).
[6] N. A. Fleck and J. W. Hutchinson, Adv. Appl. Mech. **33**, 295 (1997).
[7] N. A. Fleck and J. W. Hutchinson, J. Mech. Phys. Solids **49**, 2245 (2001).
[8] M. E. Gurtin, J. Mech. Phys. Solids **50**, 5 (2002).
[9] H. Gao, Y. Huang, W. D. Nix, and J. W. Hutchinson, J. Mech. Phys. Solids **47**, 1239 (1999).
[10] E. C. Aifantis, J. Eng. Mater. Technol. **106**, 326 (1984).
[11] L. B. Freund, J. Appl. Mech. **43**, 553 (1987).
[12] W. D. Nix, Scr. Mater. **39**, 545 (1998).
[13] W. D. Nix and O. S. Leung, Thin Films: Plasticity, Encyclopedia of Materials: Science and Technology (2001), p. 9262.
[14] P. Chaudhari, Philos. Mag. A **39**, 507 (1979).
[15] C. V. Thompson, J. Mater. Res. **8**, 237 (1993).
[16] A. Hartmaier, M. C. Fivel, G. R. Canova, and P. Gumbsch, Mater. Res. Soc. Symp. Proc. **505**, 539 (2001).
[17] M. L. Ovecoglu, D. M. Barnett, and W. D. Nix, Acta Metall. **7**, 1779 (1987).
[18] E. Van der Giessen and A. Needleman, Simul. Mater. Sci. Eng. **3**, 689 (1995).
[19] J. Y. Shu, N. A. Fleck, E. Van der Giessen, and A. Needleman, J. Mech. Phys. Solids **49**, 1361 (2001).
[20] A. N. Gulluoglu, D. J. Srolovitz, R. LeSar, and P. S. Lomdahl, Scr. Metall. **23**, 1347 (1989).
[21] L. P. Kubin, G. Canova, M. Condat, B. Devincre, V. Pontikis, and Y. Bréchet, Solid State Phenom. **455**, 23 (1992).
[22] A. Saerens, P. Van Houtte, B. Meert, and C. Quaeyhaegens, J. Appl. Crystallogr. **33**, 312 (2000).